

Heat-Treatment-Induced Switching of Magnetic States in the Doped Polar Semiconductor $\text{Ge}_{1-x}\text{Mn}_x\text{Te}$

M. Kriener,^{1,*} T. Nakajima,¹ Y. Kaneko,¹ A. Kikkawa,¹ X. Z. Yu,¹
N. Endo,² K. Kato,³ M. Takata,³ T. Arima,^{1,4} Y. Tokura,^{1,5} and Y. Taguchi¹

¹*RIKEN Center for Emergent Matter Science (CEMS), Wako 351-0198, Japan*

²*EM Business Unit, JEOL Ltd., Akishima, 196-8558, Japan*

³*RIKEN SPring-8 Center, Hyogo 679-5148, Japan*

⁴*Department of Advanced Materials Science,
University of Tokyo, Kashiwa 277-8561, Japan*

⁵*Department of Applied Physics and Quantum-Phase Electronics Center (QPEC),
University of Tokyo, Tokyo 113-8656, Japan*

(Dated: June 23, 2021)

Abstract

Cross-control of a material property – manipulation of a physical quantity (e.g., magnetisation) by a nonconjugate field (e.g., electrical field) – is a challenge in fundamental science and also important for technological device applications. It has been demonstrated that magnetic properties can be controlled by electrical and optical stimuli in various magnets. Here we find that heat-treatment allows the control over two competing magnetic phases in the Mn-doped polar semiconductor GeTe. The onset temperatures T_c of ferromagnetism vary at low Mn concentrations by a factor of five to six with a maximum $T_c \approx 180$ K, depending on the selected phase. Analyses in terms of synchrotron x-ray diffraction and energy dispersive x-ray spectroscopy indicate a possible segregation of the Mn ions, which is responsible for the high- T_c phase. More importantly, we demonstrate that the two states can be switched back and forth repeatedly from either phase by changing the heat-treatment of a sample, thereby confirming magnetic phase-change-memory functionality.

Successful cross-control of material properties has been reported or proposed for various external stimuli, such as electric field (or electric current),¹⁻³ magnetic field,^{4,5} light,⁶ and heat.⁷ Among them, heat is a particularly important stimulus since it allows for the manipulation of the state of matter through its ability to alter the free energy landscape of a system and to realize a metastable state, depending on cooling kinetics. One such example is a switching phenomenon between (atomic) amorphous and crystal phases as observed in GeTe-related materials,⁸⁻¹⁰ or between charge-glass and charge-crystal phases in organic materials,¹¹ where optical reflectivity or electrical resistivity of the system changes significantly, depending on which phase is realized (namely, depending on the cooling speed after the heat injection). This phenomenon in GeTe-related materials is applied as phase-change memory in digital versatile disks (DVD).^{9,12,13}

In addition to the phase-change memory function, GeTe exhibits various intriguing properties, such as a many-valley band structure,^{14,15} superconductivity,^{16,17} and thermoelectricity.¹⁸⁻²² The *p*-type charge carriers in this system are unintentionally self-doped due to Ge vacancies.²³ It also exhibits a ferroelectric transition at approximately 700 K, where the structure changes from its high-temperature cubic ($Fm\bar{3}m$; β -GeTe) to the low-temperature rhombohedral phase ($R3m$; α -GeTe),²⁴⁻²⁹ with a polar distortion along the cubic [111] direction [see Fig. 1 (a)]. Recently the system was predicted^{30,31} and found^{32,33} to exhibit a giant Rashba spin-splitting in the bulk, associated with broken inversion symmetry and large spin-orbit interaction.

GeTe also offers the possibility of enhanced magnetic interactions and applicability in spintronics devices: Magnetism is induced in GeTe when doping with Cr, Mn, or Fe at the Ge site,³⁴⁻³⁹ forming a family of diluted magnetic semiconductors similar with (GaMn)As or (Ga,Mn)N.⁴⁰⁻⁴⁴ Recently, the possibility of multiferroicity has been claimed in this multifunctional system due to the coexistence of magnetism and ferroelectric distortion.⁴⁵ Among the GeTe-based doped systems, $\text{Ge}_{1-x}\text{Mn}_x\text{Te}$ has been intensively studied. Single-phase GeTe–MnTe solid solutions exist over a broad range of concentration up to $x \gtrsim 0.5$.⁴⁶ The partial substitution of Ge^{2+} with iso-valent Mn^{2+} reduces the ferroelectric distortion and stabilises the cubic phase. The opposite end member MnTe is an antiferromagnet crystallizing in a different structure with the hexagonal space group $P63/mmc$. The onset temperature T_c of magnetic order was reported to increase linearly with x with maximum values around 165 K for $x = 0.5$.³⁵ More recent works have focussed on thin films of $\text{Ge}_{1-x}\text{Mn}_x\text{Te}$, finding a carrier-induced enhancement of the T_c values up to 200 K for $x = 0.08$ and hole concentrations of about $1.6 \times 10^{21} \text{ cm}^{-3}$.⁴⁶⁻⁴⁹ The emergence of ferromagnetism in bulk and thin films of $\text{Ge}_{1-x}\text{Mn}_x\text{Te}$ has been considered in an RKKY framework plus possible

antiferromagnetic correlations by Mn–Mn direct exchange.^{35,41,43}

In this Article, we focus on the low-doped region of the phase diagram $x \leq 0.2$ for bulk $\text{Ge}_{1-x}\text{Mn}_x\text{Te}$, where we found a feature which had been overlooked so far. As shown in Fig. 1 (b), there are two distinct magnetic phases, depending on the heat-treatment of the samples, with rather different values of T_c , called herein low- T_c and high- T_c phase. The origin of the high- T_c phase was identified as the formation of Mn-rich / Mn-poor regions in terms of state-of-the-art synchrotron x-ray diffraction and energy dispersive x-ray analysis. We also successfully demonstrated that samples can be repeatedly switched from the low- T_c into the high- T_c phase and vice versa by changing the heat treatment. The latter adds another interesting feature to the multifunctional semiconductor GeTe, namely magnetic phase-change-memory functionality.

Results

The magnetic phase diagram of $\text{Ge}_{1-x}\text{Mn}_x\text{Te}$ based on our present results is shown in Fig. 1 (b). The ferromagnetic transition temperature T_c is plotted against the magnetic moment at $B = 7$ T and $T = 2$ K as extracted from field-dependent magnetisation measurements (see below). The corresponding number x_m are shown on the upper horizontal axis as an effective measure of the Mn concentration. Here, x_m is calculated under the assumption that each Mn^{2+} ion with $S = 5/2$ contributes with its full moment $5 \mu_B$. The magnetic phase diagram can be divided into two sections (i) and (ii): (i) Below $x_m \sim 0.12$, there are two distinct magnetic phases with different values of T_c . Which magnetic phase is realised depends on the heat treatment of a $\text{Ge}_{1-x}\text{Mn}_x\text{Te}$ batch during growth. Quenching from the cubic phase (at 900 K) into water leads to the formation of the low- T_c phase [red open symbols in Fig. 1 (b)] while a slow and controlled cool down to room temperature, typically 5 K/h or less, establishes the high- T_c phase (blue filled symbols). In the low- T_c phase, the onset of ferromagnetism increases linearly with x . In contrast, the high- T_c phase exhibits a dome-like shape with values of T_c differing by a factor as large as five to six, compared to the low- T_c phase around $x_m \sim 0.05$, i.e., where the maximum $T_c \approx 180$ K is achieved. (ii) Above $x_m \sim 0.12$, the two different phase boundaries merge, and upon further increasing x_m , we do not observe apparent differences any more between samples from batches heat-treated in either way. As in the low- T_c phase, T_c increases linearly with x_m , although the slope is somewhat smaller than observed for $x_m \leq 0.12$.

Figure 2 summarises and compares DC- and AC-susceptibility data of samples in the low- x_m

region in panels (a) and (b), for a controlled-cooled (labelled ‘cc’) and a quenched (‘q’) sample. In the DC-susceptibility data of the lower- x_m samples in (a), the difference in the onset temperature T_c of ferromagnetism (as indicated by vertical dashed lines) between the controlled-cooled ($x_m = 0.052$, $T_c = 165$ K) and the quenched sample ($x_m = 0.049$, $T_c = 28$ K) is as much as six times despite the very similar values of x_m , which is clearly exemplified by an almost identical saturation moment of the ferromagnetic hysteresis as shown in panel (f) at $T = 2$ K. The difference in T_c is reflected in the very different behaviour of the hysteresis curves at $T = 70$ K [panel (g)], since at this temperature the quenched sample is already in its paramagnetic state. Another eminent difference in the temperature-dependent DC-susceptibility of the low- x_m samples is that the zero-field cooled (ZFC) and field-cooled (FC) data for the quenched sample are identical except at very low temperatures while there is a large difference in the case of the controlled-cooled sample below roughly $2T_c/3$. The latter resembles the behavior of a spin-glass or cluster-glass like magnetic phase while the former is closer to conventional ferromagnetic order.

To further inspect this observation, AC-susceptibility data measured on the same samples are shown in panel (b). It was measured in zero external field and at an AC excitation field of 1 Oe for various excitation frequencies $1 \text{ Hz} \leq \nu \leq 900 \text{ Hz}$. The data obtained at the lowest and the largest frequency are shown (filled symbols: $\nu = 1$ Hz, open symbols: $\nu = 900$ Hz) for the purpose of clarity. Just below T_c , a clear maximum is observed for both the controlled-cooled and the quenched sample. The frequency dependence is much more pronounced in controlled-cooled than quenched samples.

Panels (c) and (d) contain the equivalent data measured under the same conditions for a controlled-cooled ($x_m = 0.144$, $T_c = 119$ K) and a quenched sample ($x_m = 0.172$, $T_c = 124$ K) from the large- x_m part of the phase diagram. Vertical dashed lines in both panels indicate only slightly differing T_c values of each sample, which is in sharp contrast to the case of low- x_m samples. Here the FC and ZFC magnetisation data of both samples do not show any significant difference down to the lowest measurement temperature. We note that the field-dependent data taken on both higher-doped samples exhibit qualitatively similar $M(B)$ curves (not shown) as the quenched low- x_m sample. Namely, all larger- x_m samples exhibit smaller hysteresis loops similar to the low- x_m quenched samples while controlled-cooled low- x_m samples show the largest hysteresis. The AC-susceptibility data in (d) exhibits peaks below T_c , the heights of which are frequency dependent for both samples.

For a better comparison, the normalized values of the peaks are replotted against the frequency

in panel (e) on a logarithmic scale. Apparently the frequency dependence is much stronger for the controlled-cooled low- x_m sample which shows a peak suppression of about 40 %. In contrast, the three other samples exhibit a very similar frequency dependence and the respective suppression of the peaks is less than 15 %. A frequency dependence of the peak heights in AC susceptibility is a characteristic feature expected for a glass-like magnetic state.⁵⁰ Another common approach to analyse such AC susceptibility data is to examine the frequency dependence of the peak temperature T_{\max} .^{51,52} We estimated T_{\max} for the controlled-cooled sample with $x_m = 0.052$ shown in Fig. 2 (b) (blue data symbols) for all measured frequencies $1 \text{ Hz} \leq \nu \leq 900 \text{ Hz}$ and fitted the Fulcher law $\nu = \nu_0 \exp[-E_a/k_B(T_{\max}(\nu) - T_0)]$ to these data as described in Ref. 51. Although the fit result (not shown) is not perfect at low frequencies, it describes well the data at higher frequencies and resembles the behavior reported for metallic RKKY-spin glasses rather than systems in which the spin glass phase emerges due to geometrical frustration.⁵¹

All the AC- and DC-magnetic data taken together, the controlled-cooled low- x_m sample exhibits a more spin-glass-like or clustered magnetic structure while the magnetic phases of both larger- x_m and the low- x_m quenched samples are similar to an ordinary ferromagnet. One possible scenario is a segregation of the magnetic Mn ions in the low- x_m high- T_c sample during the controlled-cooling process. The high- T_c phase is characterized by Mn-rich islands or clusters embedded into a lake or matrix of relatively Mn-poor GeTe, as it is expected if a spinodal decomposition occurs,^{41,53,54} while the low- T_c phase consists of a more homogeneous Mn distribution.

To test this scenario and further characterize the different magnetic phases, we carried out a high-resolution x-ray diffraction study employing synchrotron radiation with the wavelength of $0.5001(1) \text{ \AA}$. The main result is shown in Fig. 3. As before, controlled-cooled and quenched powder samples from both the low- x_m and the large- x_m sections in the phase diagram were analysed: The differences in the magnetic phases are reflected in differences in the XRD patterns. Figures 3 (a) to (d) show XRD data for four selected samples on a magnified view of the cubic 220_c reflection around $2\theta \sim 13.5^\circ$: (a) $x_m = 0.050$, $T_c = 24 \text{ K}$, quenched; (b) $x_m = 0.047$, $T_c = 171 \text{ K}$, controlled cooled; (c) $x_m = 0.166$, $T_c = 125 \text{ K}$, quenched; (d) $x_m = 0.164$, $T_c = 127 \text{ K}$, controlled cooled. In quenched low- x_m samples as shown in Fig. 3 (a), we observe two comparably sharp peaks indexable as the 104_h and 110_h reflections in hexagonal setting, which are expected for the polar rhombohedrally-distorted GeTe phase. For large- x_m samples [Fig. 3 (c) and (d)] above the structural phase transition [shaded areas in Figs. 1 (b) and 3 (e)], there is only one comparably sharp peak, irrespective of the heat treatment, which is indexable as the corresponding 220_c reflec-

tion in the cubic GeTe phase. This is in agreement with the observation that for $x_m > 0.12$, there is no clear difference in the magnetic state any more between controlled-cooled and quenched samples.

However, for controlled-cooled samples with smaller x_m , i.e., below the grey-shaded area in the phase diagram, the situation turns out to be much more complicated. As can be seen in panel (b), the 104_h reflection has split into two broader peaks with lower intensity. We note that we also observe similar splittings of other reflections (hkl_h) with non-zero l_h value, indicating that this splitting is not due to an impurity phase. At the same time the 110_h peak also broadens. Keeping in mind that the 104_h reflection provides information about the degree of the rhombohedral distortion, we interpret the apparent double-peak structure as an indication that controlled-cooled low- x_m sample consists of domains with different degrees of rhombohedral distortion while obeying the same overall crystal symmetry. In the present case, we assume domains with two main distortions and label the two peaks in Fig. 3 (b) as ‘ $R1$ ’ and ‘ $R2$ ’ for simplicity. The former domain $R1$ is strongly distorted, close to the situation in pristine GeTe while the latter exhibits a smaller distortion which implies that the $R2$ component has a larger Mn concentration, naturally supporting the aforementioned scenario of a slow-cooling triggered spatial inhomogeneity of the Mn distribution.

In Fig. 3 (e), the estimated lattice constants for these four samples and additional quenched samples are plotted against x_m in pseudo-cubic setting for a better comparability. The c_h parameter of quenched samples shrinks pronouncedly while a_h increases slightly with x_m . In the ‘real’ cubic phase for $x_m \gtrsim 0.12$, the lattice parameter shrinks. In the controlled-cooled low- x_m sample [Fig. 3 (b)], the single lattice parameter a_h (common to the $R1$ and $R2$ phases) as estimated from the 110_h reflection is plotted with a filled ball symbol, fitting into the systematic change of the d spacing perpendicular to the polar axis. Due to the peak splitting, we estimated the lattice parameters c_h for each of the two 104_h reflections $R1$ and $R2$ as denoted by filled square symbols in panel (e). The difference in the degree of the rhombohedral distortion is reflected in two very different lengths of c_h . As expected, above the structural phase transition there is no difference between samples treated by either cooling recipe.

As a next step, we carried out an energy-dispersive x-ray (EDX) analysis by using a scanning transmission electron microscope (STEM) to probe and visualize the spatial Mn distribution in two samples from the low- x_m section of the phase diagram. The resulting EDX mappings of Mn count are shown in Fig. 4 (a) for a controlled-cooled sample ($x_m = 0.054$, $T_c = 167$ K) and in (c)

for a quenched sample ($x_m = 0.076$, $T_c = 45$ K). Figures 4 (b) and (d) show the average atomic percentage of Mn ions from ten line scans taken around the white dashed lines in panels (a) and (c). Clearly, the controlled-cooled sample exhibits a much more inhomogeneous Mn distribution than the quenched sample, although the quenched sample also shows a slight inhomogeneity. This finding is in accord with the observations made in relation to magnetic and XRD data. The characteristic length scale of the Mn clustering amounts to several tens of nm, as seen in Figs. 4 (a) and (b).

Another important issue is whether the different magnetic phases with high- T_c and low- T_c values in the low- x_m section of the magnetic phase diagram can be repeatedly switched back and forth. To demonstrate this feature, a sample from an initially controlled-cooled batch ($x_m = 0.045$) was chosen and six times (from step 2 to step 7) switched as shown in Fig. 5 (a). The T_c values are replotted in panel (b) as a function of the heat-treatment step, along with the magnetisation value at 70 K in Fig. 5 (c) as indicated by the vertical line in panel (a). For either data set, open symbols refer to measurements on quenched and filled symbols to controlled-cooled samples. This finding indicates that both observed magnetic phases are reproducibly switchable into each other, fulfilling one of the essential requirements for phase-change-memory functionality. It should be noted that the slight variation in T_c of the high- T_c phase between the different phase switching steps 1, 3, 5, and 7 shown in Fig. 5 is probably a consequence of slightly different degrees of Mn inhomogeneity in the sample obtained after each thermal cycle, rather than due to a degradation in the bulk of the sample.

Discussion

The present data provide a consistent picture suggesting that the difference in the strength of ferromagnetic interaction originates from the degree of clustering or inhomogeneity of the substitutionally doped Mn^{2+} ions. On the one hand, high T_c values are found when the Mn-rich clusters or islands in a lake of Mn-poor, almost pristine GeTe have the time to arrange themselves during the controlled-cooling process, i.e., for x_m around 0.05 leading to a highly inhomogeneous situation. Within the Mn-rich region, the ferromagnetic interaction is stronger than expected for the averaged Mn concentration within the RKKY scheme. On the other hand, when the Mn ions are not able to cluster, i.e., when the system is quenched from the high-temperature homogeneous arrangement, the T_c values turn out to be much smaller. Apparently, the homogeneous situation

is frozen and the magnetic interaction is weaker. Upon further doping, the Mn concentration becomes large enough to allow for cubic phase fractions to emerge. This leads to a suppression of T_c when approaching the critical x_m range around ≈ 0.12 where the structural phase transition drops below room temperature. Hence the high- T_c and low- T_c phase boundaries merge and the clustering is reduced. One might expect that at sufficiently large Mn-doping concentrations, similarly large T_c values must be achievable. In fact, the maximum T_c was reported in the old literature to be around 160 K for $x \sim 0.5$,³⁵ somewhat smaller than $T_c = 180$ K reported in this Article. Assuming that the slope of the phase boundary above $x_m \sim 0.12$ holds and extrapolating the phase line towards larger x_m values, a comparably large T_c of 180 K is expected for $x_m \sim 0.4$ in the cubic phase. However, even the local spatial fluctuation of the Mn content for the low- x_m and high- T_c sample [see Fig. 4(b)] seems not to reach such a high value as $x_m \sim 0.4$ (cubic). This discrepancy may have the important implication that the possible accommodation of relatively high- x_m ($\gtrsim 0.1$) Mn content in the rhombohedrally distorted polar lattice structure (e.g., the $R2$ phase in Fig. 3) may host higher T_c values than the comparably or even higher Mn-doped cubic phase. The characteristic Rashba-type spin-split valence band structure in the polar state, as recently proven theoretically^{30,31} and experimentally,^{32,33} may play some role in giving rise to such a large difference in RKKY interactions in the polar and cubic lattices.

The appearance of Mn inhomogeneity and different rhombohedral distortions in this system suggest that a spinodal decomposition occurs in the low-Mn-concentration region when a sample is cooled down slowly: A uniform solid solution becomes unstable against composition modulations upon cooling.⁵³⁻⁵⁵ We note here that this process is totally different from the structural phase change between crystalline and amorphous. The highest temperature which the samples experience during the heat-treatment process is 900 K, which is well below the melting temperature of $\text{Ge}_{1-x}\text{Mn}_x\text{Te}$. Such a nanoscale phase separation is discussed in related compounds, and means that the spin subsystems undergo a segregation, i.e., regions with an either high or low concentration of the magnetic dopant are formed. It is also known that the degree of inhomogeneity in diluted magnetic semiconductors can indeed influence the strength of the ferromagnetic interaction and strong inhomogeneity may significantly increase T_c .^{53,56} Moreover it was reported that the ferromagnetic transition temperature can vary depending on the heat-treatment, as, e.g., in the text-book diluted magnetic semiconductor $(\text{Ga,Mn})\text{As}$,⁴⁰ but the mechanism is different from the spinodal decomposition proposed here for. In the case of $(\text{Ga,Mn})\text{As}$, the annealing largely affects the amount of interstitial Mn ions, resulting in the difference of T_c . In the present case, however,

the almost identical properties in the high- x_m region among the samples treated in either thermal process indicate that interstitial Mn ions, if any, play a rather minor role in governing the magnetic properties (although the effect of interstitial Mn ions should be investigated in detail in the future). Therefore, the magnetic phase change functionality reported here was never identified before.

It was theoretically found that nanoscale spinodal decomposition in diluted magnetic semiconductors can lead to large values of T_c in cases where there is only a short-range magnetic exchange interaction.^{53,57} We speculate that the high- T_c values reported for thin films⁴⁷⁻⁴⁹ are actually belonging to the here-reported bulk high- T_c phase (while the low- T_c phase line is probably the one which was observed and reported in the old literature Ref. 35). High T_c values are only reported for thin films with small x which were grown at comparably low temperatures < 620 K,^{48,49} i.e., in the same temperature window which was found in this study to trigger the formation of the high- T_c phase in our samples. Therefore the proposed spinodal decomposition mechanism is probably the intrinsic origin for the existence of the high- T_c magnetic phase in $\text{Ge}_{1-x}\text{Mn}_x\text{Te}$. Another interesting issue is the size of the Mn clusters formed due to the spinodal decomposition. For bulk $\text{Ge}_{1-x}\text{Mn}_x\text{Te}$ we estimated an average Mn cluster size to be several tens of nanometers by employing Scherrer's formula to the broadened XRD patterns of controlled-cooled powder samples with large T_c values. We also estimated the mean-free path of a sample with $x \approx 0.09$, high- T_c phase, from preliminary transport measurements. The mean-free path is smaller than 10 nm and this makes sense since the enhancement of T_c could not occur if the Mn cluster size were smaller than the mean-free path and the inhomogeneity of the Mn concentration were averaged out. This is an interesting starting point for future studies on the ferromagnetism realised in $\text{Ge}_{1-x}\text{Mn}_x\text{Te}$.

One might speculate whether it could also be possible to gain control over the magnetic-phase-switching process by electronic means, i.e., whether it is possible to switch the magnetic phases by electric fields utilising the ferroelectric distortion which sets in upon cooling through ~ 700 K. Unfortunately the semiconductor GeTe is a fairly good metal with room-temperature values of the longitudinal resistivity of a few $100 \mu\Omega\text{cm}$ and unintentionally self-doped charge carrier concentrations n of the order of 10^{21} cm^{-3} . To drive the magnetic phase change by electrical fields, one has to reduce n . Mn doping alone does not seem to reduce n sufficiently, at least in the doping range in question, i.e., $x_m \lesssim 0.12$. In general, the role of the density of the self-doped charge carriers in $\text{Ge}_{1-x}\text{Mn}_x\text{Te}$ remains an open question. In diluted magnetic semiconductors, the ferromagnetic interaction is generally believed to depend on the charge carrier concentration,^{43,57} which was also reported for thin films of $\text{Ge}_{1-x}\text{Mn}_x\text{Te}$.⁵⁸

In conclusion we report the finding that a different heat treatment (quenching vs. slow cooling) results in either of two competing ferromagnetic phases with significantly different ordering temperatures T_c in the bulk diluted magnetic semiconductor $\text{Ge}_{1-x}\text{Mn}_x\text{Te}$. The high- T_c phase partly resembles a spin- or cluster-glass state with maximum ordering temperatures of up to ~ 180 K around $x_m \sim 0.05$ which had not been reported before. It is characterized by an inhomogeneous distribution of the doped Mn^{2+} ions due to a spinodal decomposition taking place upon slow cooling from above the ferroelectric transition temperature (~ 700 K). The low- T_c phase is more homogeneous and closer to conventional ferromagnetic order. The two phases merge around $x_m \approx 0.12$. At the same time the ferroelectric lattice distortion vanishes. Moreover, it was demonstrated that repeated switching back and forth between the two distinct phases is possible by either quenching (high- T_c to low- T_c) or controlled cooling (low- T_c to high- T_c). This adds another interesting feature to the intriguing semiconductor GeTe in terms of a magnetic phase-change-memory functionality.

Methods

Sample Preparation and Characterization. Polycrystals of $\text{Ge}_{1-x}\text{Mn}_x\text{Te}$ for nominally $0 \leq x < 0.2$ were grown by conventional melt growth and Bridgman methods. Stoichiometric mixtures of GeTe (purity: 5N) and MnTe (3N+) were thoroughly mixed and sealed into evacuated quartz glass tubes. In the conventional melt growth runs, the batches were heated to 1073 - 1123 K (melting point of GeTe: $T_m \approx 1000$ K; upon Mn doping it gradually increases to $T_m \approx 1073$ K for $x \approx 0.5$ ⁵⁹), kept there for 12–24 h and subsequently cooled down to approximately 900 K which is still in the cubic high-temperature phase for all samples examined here (GeTe: $T_{\text{struct}} \approx 700$ K; upon Mn doping T_{struct} decreases). Then the batches were (i) slowly cooled (5 K/h) to room temperature or (ii) quenched into water. In the Bridgman growth method, the upper heater was set to 1123 K and the lower to 623 K. The mixed powder was kept at the upper heater’s temperature for 12–24 h. Then the batch was slowly lowered (2 mm/h) from the upper heater towards the lower heater and again (i) slowly cooled down, or (ii) the quartz tubes were quenched when the batch position corresponded to approximately 900 K. We tried different annealing times at 900 K without finding any impact on the magnetic phase, which implies that the relevant temperature range for the clustering process during the slow-cooling process is below that temperature. There is always a slight gradient of the Mn concentration in batches grown by either recipe / method. Therefore, for small samples cut or broken from an as-grown batch, the magnetization moment at

$T = 2$ K and $B = 7$ T is used to estimate the Mn concentration effectively. This approach was verified for selected samples by chemical composition determination using a SEM-EDX apparatus (JEOL JCM-2000).

Measurement. DC-magnetisation and AC-susceptibility data were measured with commercial magnetometers (MPMS XL and MPMS-3, Quantum Design). The synchrotron radiation experiments were performed at BL44B2 in SPring-8 with the approval of RIKEN (Proposal No. 20150045), and with a commercial in-house apparatus (RIGAKU). Scherrer's formula $L = K\lambda/(\Delta_{2\theta} \cos(\theta))$ was used to estimate the Mn cluster size L from the peak width. Here $K \approx 1$ is a form factor, λ the wave length of the used radiation, and θ the Bragg angle. STEM-EDX data was taken at JEOL Ltd. by employing a JEM-2800 apparatus. The onset temperature of ferromagnetism is defined as the initial linear slope as indicated in Figs. 2 (a) and (c) and 5 (a) by dashed lines. The software VESTA was used for the structure plot in Fig. 1 (a), see Ref. 60.

* corresponding author: markus.kriener@riken.jp

- ¹ F. Matsukura, Y. Tokura, and H. Ohno, *Nat. Nanotechnol.* **10**, 209 (2015).
- ² S. S. P. Parkin, M. Hayashi, and L. Thomas, *Science* **320**, 190 (2008).
- ³ A. Yamaguchi, T. Ono, S. Nasu, K. Miyake, K. Mibu, and T. Shinjo, *Phys. Rev. Lett.* **92**, 077205 (2004).
- ⁴ Y. Tokura, *Rep. Prog. Phys.* **69**, 797 (2006).
- ⁵ Y. Tokura, S. Seki, and N. Nagaosa, *Rep. Prog. Phys.* **77**, 076501 (2014).
- ⁶ A. Kirilyuk, A. V. Kimel, and T. Rasing, *Rev. Mod. Phys.* **82**, 2731 (2010).
- ⁷ W. Koshibae and N. Nagaosa, *Nat. Commun.* **5**, 5148 (2014).
- ⁸ M. Chen, K. A. Rubin, and R. W. Barton, *Appl. Phys. Lett.* **49**, 502 (1986).
- ⁹ D. Lencer, M. Salinga, B. Grabowski, T. Hickel, J. Neugebauer, and M. Wuttig, *Nat. Mater.* **7**, 972 (2008).
- ¹⁰ X. Q. Liu, X. B. Li, L. Zhang, Y. Q. Cheng, Z. G. Yan, M. Xu, X. D. Han, S. B. Zhang, Z. Zhang, and E. Ma, *Phys. Rev. Lett.* **106**, 025501 (2011).
- ¹¹ H. Oike, F. Kagawa, N. Ogawa, A. Ueda, H. Mori, M. Kawasaki, and Y. Tokura, *Phys. Rev. B* **91**, 041101(R) (2015).
- ¹² A. P. J. M. Jongenelis, J. H. Coombs, W. van Es-Spiekman, and B. A. J. Jacobs, *J. Appl. Phys.* **79**, 8349 (1996).

- ¹³ A. V. Kolobov, D. J. Kim, A. Giussani, P. Fons, J. Tominaga, R. Calarco, and A. Gruverman, *APL Mater.* **2**, 066101 (2014).
- ¹⁴ F. Herman, R. L. Kortum, I. B. Ortenburger, and J. P. van Dyke, *J. Phys. Colloques* **29**, C4 (1968).
- ¹⁵ A. Ciucivara, B. R. Sahu, and L. Kleinman, *Phys. Rev. B* **73**, 214105 (2006).
- ¹⁶ M. Cohen, *Phys. Rev.* **134**, A511 (1964).
- ¹⁷ R. Hein, J. Gibson, R. Mazelsky, R. Miller, and J. Hulm, *Phys. Rev. Lett.* **12**, 320 (1964).
- ¹⁸ G. J. Snyder and E. S. Toberer, *Nat. Mater.* **7**, 105 (2008).
- ¹⁹ E. M. Levin, M. F. Besser, and R. Hanus, *Appl. Phys. Lett.* **114**, 083713 (2013).
- ²⁰ J. Davidow and Y. Gelbstein, *J. Solid State Chem.* **42**, 1542 (2013).
- ²¹ J. K. Lee, M. W. Oh, B. S. Kim, B. K. Min, H. W. Lee, and S. D. Park, *Electron. Mater. Lett.* **10**, 813 (2014).
- ²² D. Wu, L.-D. Zhao, S. Hao, Q. Jiang, F. Zheng, J. W. Doak, H. Wu, H. Chi, Y. Gelbstein, C. Uher, C. Wolverton, M. Kanatzidis, and J. He, *J. Am. Chem. Soc.* **136**, 11412 (2014).
- ²³ A. H. Edwards, A. C. Pineda, P. A. Schultz, M. G. Martin, A. P. Thompson, H. P. Hjalmarson, and C. J. Umrigar, *Phys. Rev. B* **73**, 045210 (2006).
- ²⁴ J. Goldak, C. S. Barrett, D. Innes, and W. Youdelis, *J. Chem. Phys.* **44**, 3323 (1966).
- ²⁵ G. S. Pawley, W. Cochran, R. A. Cowley, and G. Dolling, *Phys. Rev. Lett.* **17**, 753 (1966).
- ²⁶ T. Chattopadhyay, J. X. Boucherle, and H. G. von Schnering, *J. Phys. C: Solid State Phys.* **20**, 1431 (1987).
- ²⁷ K. M. Rabe and J. D. Joannopoulos, *Phys. Rev. B* **36**, 6631 (1987).
- ²⁸ A. Schlieper, Y. Feutelais, S. G. Fries, B. Legendre, and R. Blachnik, *Calphad* **23**, 1 (1999).
- ²⁹ P. Fons, A. V. Kolobov, M. Krbal, J. Tominaga, K. S. Andrikopoulos, S. N. Yannopoulos, G. A. Voyiatzis, and T. Uruga, *Phys. Rev. B* **82**, 155209 (2010).
- ³⁰ D. D. Sante, P. Barone, R. Bertacco, and S. Picozzi, *Adv. Mater.* **25**, 509 (2013).
- ³¹ S. Picozzi, *Front. Physics* **2**, 10 (2014).
- ³² C. Rinaldi, D. D. Sante, A. Giussani, R.-N. Wang, S. Bertoli, M. Cantoni, L. Baldrati, I. Vobornik, G. Panaccione, R. Calarco, S. Picozzi, and R. Bertacco, arXiv:1412.2386v1 (2014).
- ³³ J. Krempaský, H. Volfová, S. Muff, N. Pilet, G. Landolt, M. Radović, M. Shi, D. Kriegner, V. Holý, J. Braun, H. Ebert, F. Bisti, V. A. Rogalev, V. N. Strocov, G. Springholz, J. Minár, and J. H. Dil, arXiv:1503.05004v1 (2015).
- ³⁴ M. Rodot, J. Lewis, H. Rodot, G. Villers, J. Cohen, and P. Mollard, *J. Phys. Soc. Jap. Suppl.* **21**, 627

- (1966).
- ³⁵ R. W. Cochrane, M. Plischke, and J. O. Ström-Olsen, *Phys. Rev. B* **9**, 3013 (1974).
- ³⁶ Y. Fukuma, N. Nishimura, H. Asada, and T. Koyanagi, *Physica E* **10**, 268 (2001).
- ³⁷ Y. Fukuma, H. Asada, J. Miyashita, N. Nishimura, and T. Koyanagi, *J. Appl. Phys.* **93**, 7667 (2003).
- ³⁸ W. Knoff, K. Świątek, T. Andrearczyk, V. Domukhovski, P. Dziawa, L. Kowalczyk, E. Lusakowska, A. Šiušys, B. Taliashvili, J. Wróbel, and T. Story, *Phys. Status Solidi B* **248**, 1605 (2011).
- ³⁹ F. Tong, J. H. Hao, Z. P. Chen, G. Y. Gao, and X. S. Miao, *Appl. Phys. Lett.* **99**, 081908 (2011).
- ⁴⁰ T. Jungwirth, K. Y. Wang, J. Mašek, K. W. Edmonds, J. König, J. Sinova, M. Polini, N. A. Goncharuk, A. H. MacDonald, M. Sawicki, A. W. Rushforth, R. P. Campion, L. X. Zhao, C. T. Foxon, and B. L. Gallagher, *Phys. Rev. B* **72**, 165204 (2005).
- ⁴¹ T. Dietl, *Nat. Mater.* **9**, 965 (2010).
- ⁴² L. Chen, X. Yang, F. Yang, J. Zhao, J. Misuraca, P. Xiong, and S. von Molnár, *Nano Lett.* **11**, 2584 (2011).
- ⁴³ T. Dietl and H. Ohno, *Rev. Mod. Phys.* **86**, 187 (2014).
- ⁴⁴ M. Tanaka, S. Ohya, and P. N. Hai, *Appl. Phys. Rev.* **1**, 011102 (2014).
- ⁴⁵ H. Przybylińska, G. Springholz, R. T. Lechner, M. Hassan, M. Wegscheider, W. Jantsch, and G. Bauer, *Phys. Rev. Lett.* **112**, 047202 (2014).
- ⁴⁶ R. T. Lechner, G. Springholz, M. Hassan, H. Groiss, R. Kirchschrager, J. Stangl, N. Hrauda, and G. Bauer, *Appl. Phys. Lett.* **97**, 023101 (2010).
- ⁴⁷ W. Q. Chen, S. T. Lim, C. H. Sim, J. F. Bi, K. L. Teo, T. Liew, and T. C. Chong, *J. Appl. Phys.* **104**, 063912 (2008).
- ⁴⁸ Y. Fukuma, H. Asada, S. Miyawaki, T. Koyanagi, S. Senba, K. Goto, and H. Sato, *Appl. Phys. Lett.* **93**, 252502 (2008).
- ⁴⁹ M. Hassan, G. Springholz, R. T. Lechner, H. Groiss, R. Kirchschrager, and G. Bauer, *J. Crystal Growth* **323**, 363 (2011).
- ⁵⁰ K. Binder and A. Young, *Rev. Mod. Phys.* **58**, 801 (1986).
- ⁵¹ J. L. Tholence, *Solid-State Commun.* **35**, 113 (1980).
- ⁵² H. Aruga, T. Tokoro, and A. Ito, *J. Phys. Soc. Jpn.* **57**, 261 (1988).
- ⁵³ K. Sato, H. Katayama-Yoshida, and P. H. Dederichs, *Jpn. J. Appl. Phys.* **44**, L948 (2005).
- ⁵⁴ T. Dietl, K. Sato, T. Fukushima, A. Bonanni, M. Jamet, A. Barski, S. Kuroda, M. Tanaka, P. N. Hai, and H. Katayama-Yoshida, *Rev. Mod. Phys.* **87**, 1311 (2015).

- ⁵⁵ Z. Hiroi, H. Hayamizu, T. Yoshida, Y. Muraoka, Y. Okamoto, J. Yamaura, and Y. Ueda, *Chem. Mater.* **25**, 2202 (2013).
- ⁵⁶ M. Jamet, A. Barski, T. Devillers, V. Poydenot, R. Dujardin, P. Bayle-Guillevaud, J. Rothman, E. Bellet-Amalric, A. Marty, J. Cibert, R. Mattana, and S. Tatarenko, *Nat. Mater.* **5**, 653 (2006).
- ⁵⁷ H. Katayama-Yoshida, K. Sato, T. Fukushima, M. Toyoda, H. Kizaki, V. A. Dinh, and P. H. Dederichs, *Phys. Status Solidi A* **204**, 15 (2007).
- ⁵⁸ Y. Fukuma, H. Asada, M. Arifuku, and T. Koyanagi, *Appl. Phys. Lett.* **80**, 1013 (2002).
- ⁵⁹ W. D. Johnston and D. E. Sestrich, *J. Inorg. Nucl. Chem.* **19**, 229 (1961).
- ⁶⁰ K. Momma and F. Izumi, *J. Appl. Crystallogr.* **44**, 1272 (2011).

Acknowledgments

This work is supported by a Grants-in-Aid for Scientific Research (S) from the Japan Society for the Promotion of Science (JSPS, No. 24224009). MK is supported by a Grants-in-Aid for Young Scientists (B) (JSPS, KAKENHI No. 25800197) and by a Grants-in-Aid for Scientific Research (C) (JSPS, KAKENHI No. 15K05140).

Figures

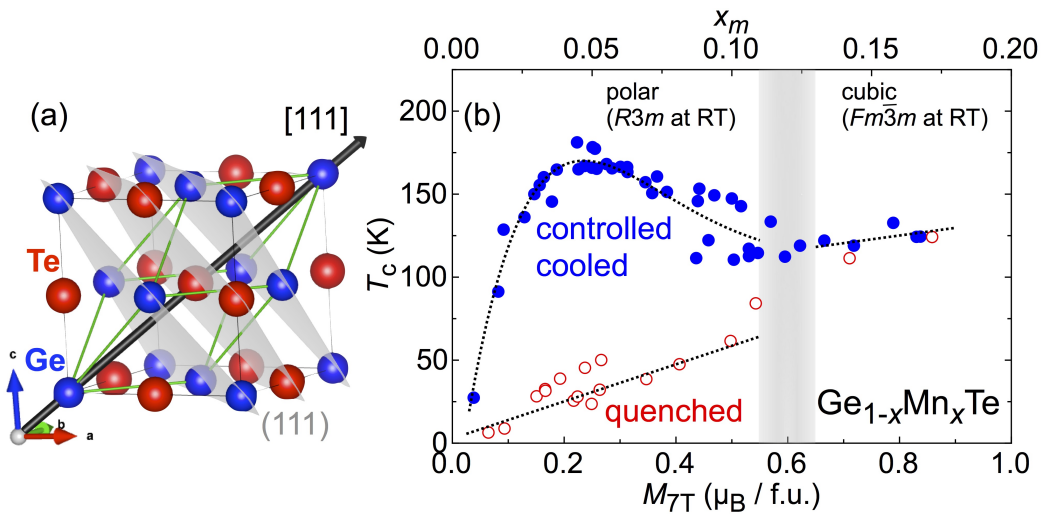


FIG. 1: Structure and phase diagram of $\text{Ge}_{1-x}\text{Mn}_x\text{Te}$: (a) Structural plots depicting the high-temperature cubic and the low-temperature rhombohedrally-distorted GeTe structure superimposed in its pseudo-cubic setting. The high-temperature structure is of rock-salt type. The atoms Ge (blue), Te (red), and the crystallographic (111) planes (grey) are indicated. The black arrow depicts the cubic [111] direction, along which the polar distortion occurs. (b) Magnetic phase diagram of $\text{Ge}_{1-x}\text{Mn}_x\text{Te}$. Horizontal axis is magnetisation value at 2 K and 7 T, which is an effective measure of the Mn concentration. The corresponding number x_m is plotted at the upper horizontal axis. Filled symbols (blue) refer to the onset of ferromagnetism in controlled-cooled samples, open symbols (red) to quenched samples; see the Methods section for the details of the heat-treatment procedures. The grey shaded area highlights the x_m range where the structural phase transition from rhombohedral to cubic phase drops below room temperature. Dotted lines are guides to the eyes.

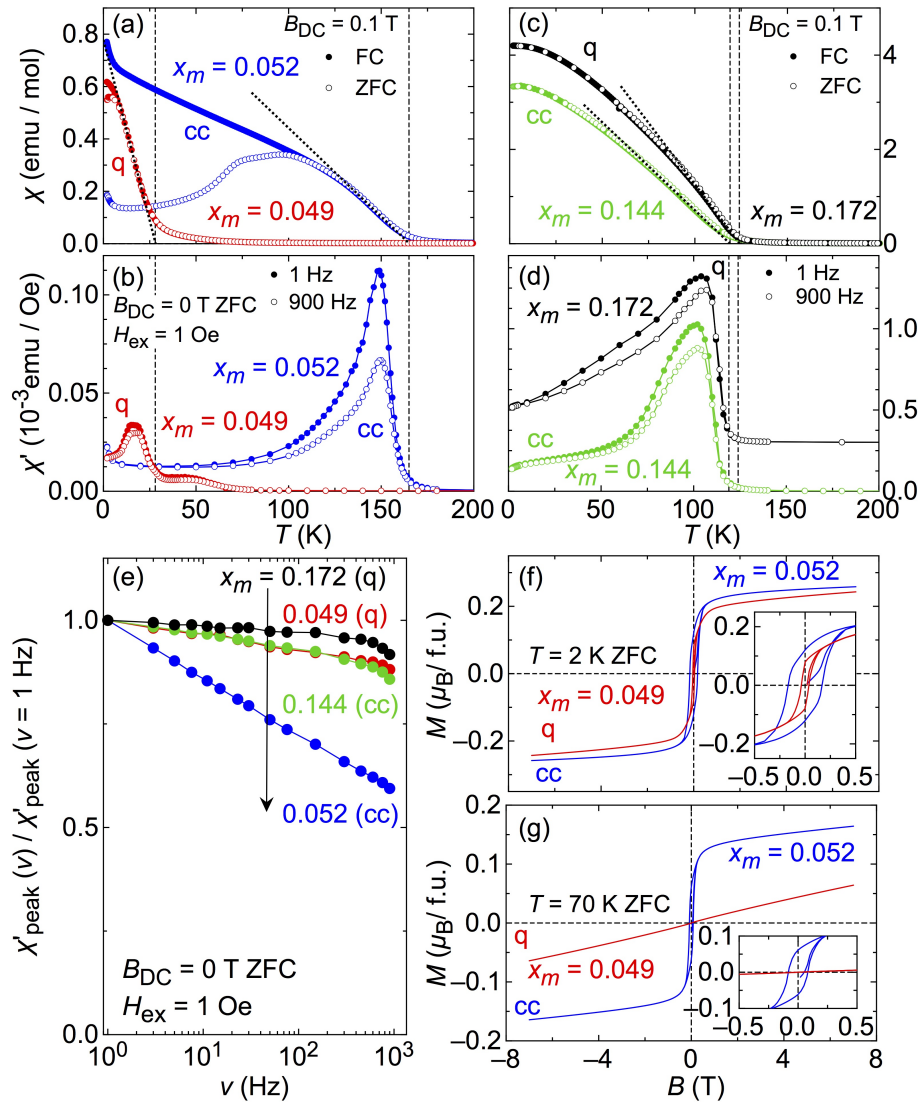


FIG. 2: Magnetisation data of $\text{Ge}_{1-x}\text{Mn}_x\text{Te}$: (a) DC- and (b) AC-susceptibility data for a controlled-cooled ($x_m = 0.052$; blue symbols) and a quenched sample ($x_m = 0.049$, red symbols) in the low- x_m region of the phase diagram. (c) and (d) show the respective data for samples with higher x_m (controlled cooled: $x_m = 0.144$, green symbols, and quenched: $x_m = 0.172$, black symbols). In panels (a) and (c) filled symbols are measured in field-cooling (FC) runs and open symbols denote data measured after zero-field cooling (ZFC). The dotted lines are fits to the data and show how the magnetic transition temperatures T_c were estimated. The vertical lines in (a)–(d) indicate thus determined T_c values. The AC-susceptibility data in panels (b) and (d) were taken in zero DC magnetic fields and an AC excitation field of 1 Oe. Closed symbols in both panels refer to data taken at an excitation frequency ν of 1 Hz (lowest applied ν), open symbols to data taken in 900 Hz (largest applied ν). The data of the quenched sample in (d) are shifted vertically for clarity. In (e), the frequency dependence of the normalized peak value χ' for all four samples are summarized, with the horizontal axis in logarithmic scale. Panels (f) and (g) show field-dependent magnetisation data at 2 K and 70 K, respectively. The insets are an expanded view around the origin.

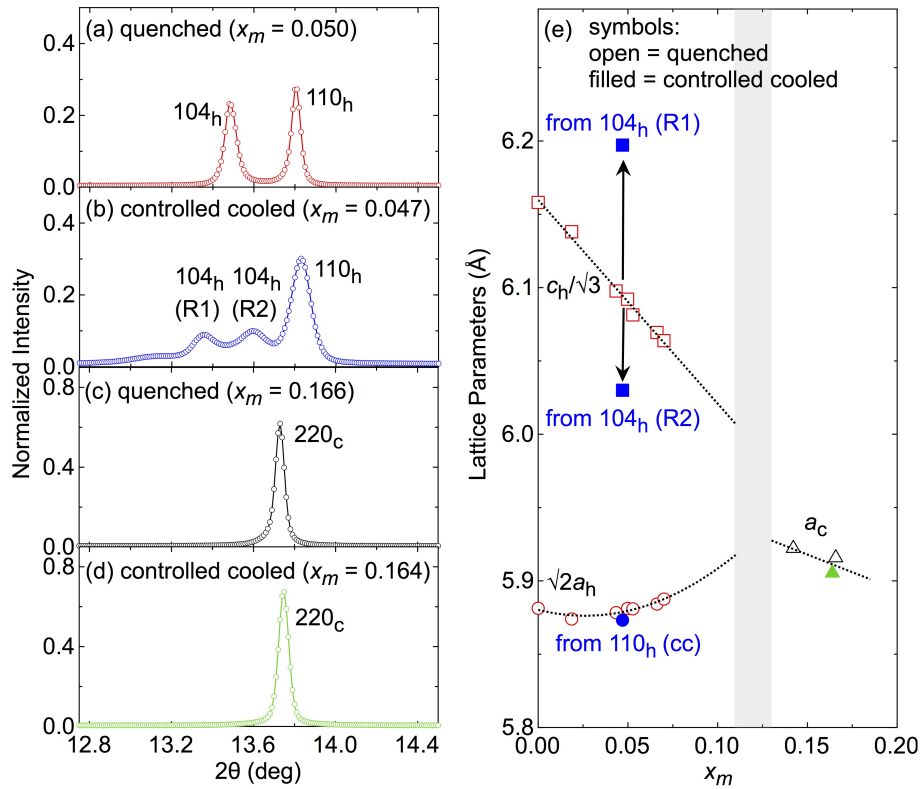


FIG. 3: XRD data of $\text{Ge}_{1-x}\text{Mn}_x\text{Te}$: Data are shown for four different samples around the single cubic (220) peak and the corresponding (104) and (110) reflections (hexagonal setting) that are split due to the polar distortion: (a) quenched sample with $x_m = 0.050$, (b) controlled-cooled sample with $x_m = 0.047$, (c) quenched, $x_m = 0.166$, and (d) controlled cooled, $x_m = 0.164$. (e) Lattice constants as estimated from the XRD data for these and additional quenched samples. Filled symbols refer to controlled-cooled, open symbols to quenched samples. The two data points labelled R1 and R2 refer to the c_h lattice constants estimated for the two 104_h peaks labeled in the same way in panel (b), see text. The filled circle denotes the corresponding a_h lattice constant. The lattice parameters in hexagonal setting a_h and c_h transform into the pseudo-cubic setting (\tilde{a}_c, \tilde{c}_c) as follows: $\tilde{a}_c = \sqrt{2}a_h$ and $\tilde{c}_c = c_h/\sqrt{3}$, and $\sqrt{2}a_h$ and $c_h/\sqrt{3}$ are plotted for a better comparability.

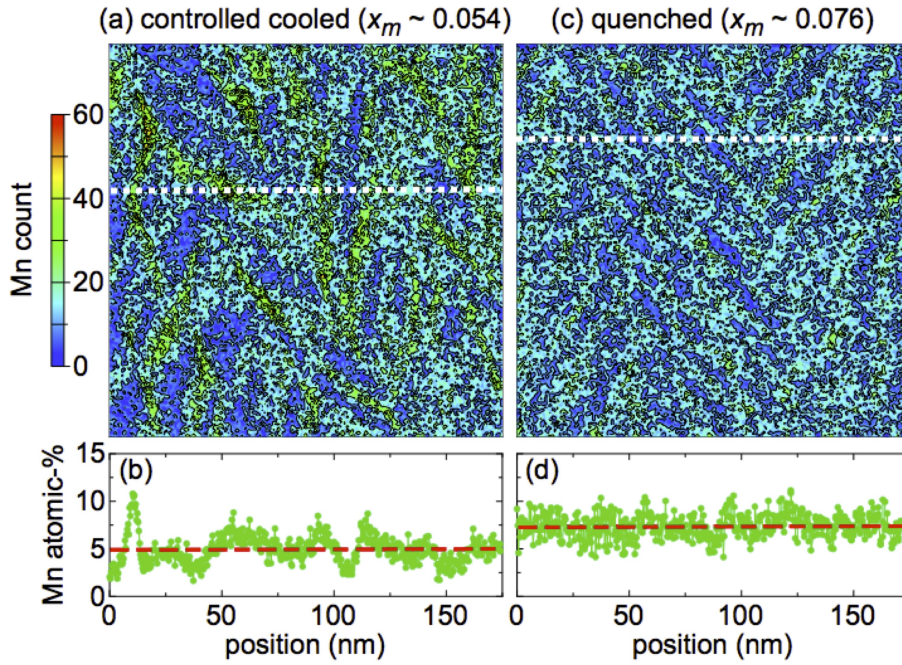


FIG. 4: EDX data of $\text{Ge}_{1-x}\text{Mn}_x\text{Te}$: Comparison of EDX images (Mn count) of (a) a controlled-cooled sample with a Mn concentration of $x_m = 0.054$ and (b) a quenched sample, $x_m = 0.076$. The size of the view area of (a) and (c) is $170 \times 170 \text{ nm}^2$. The white dashed lines denote the approximate position of the line scans shown in panels (b) and (d), respectively, for the two samples. In (b) and (d), the average Mn concentrations along these line scans are indicated by a red dashed line, which show good agreement with the respective x_m values. The controlled-cooled sample exhibits a more inhomogeneous Mn distribution than the quenched sample, see text.

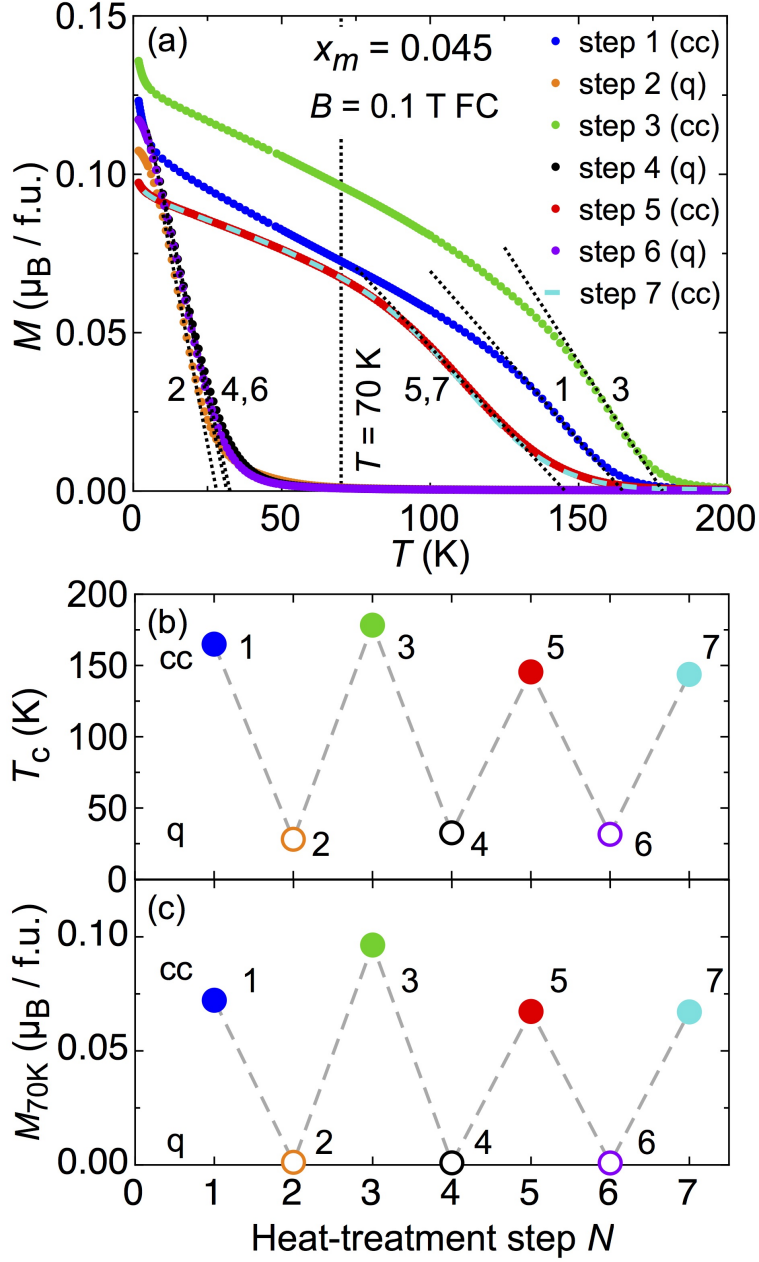


FIG. 5: Demonstration of phase switching in $\text{Ge}_{1-x}\text{Mn}_x\text{Te}$: (a) summarizes DC magnetisation data for each of the seven phase-conversion steps (controlled cooled ‘cc’ vs. quenched ‘q’). All data are taken on the same specimen upon field cooling in $B = 0.1 \text{ T}$. The Mn concentration as estimated from the magnetisation value at 2 K and 7 T is $x_m = 0.045$. The dotted lines are fits to the data and show how the magnetic transition temperatures T_c were determined. The numbers 1 to 7 indicate the chronological order of the heat treatment and hence measurements. The variation of T_c and the magnetisation at 70 K as indicated by the vertical line in (a) among the different switching steps are shown in (b) and (c), respectively.